Inverse problems

Elasticity reconstruction: Beyond the assumption of local homogeneity

Ralph Sinkus [a],[*], Jean-Luc Daire [b], Bernard E. Van Beers [b], Valerie Vilgrain [b]

[a] *Institut Langevin, ESPCI, 10, rue Vauquelin, 75005 Paris, France*
[b] *Centre de recherches biomédicales Bichat-Beaujon, 75018 Paris, France*

A B S T R A C T

Elasticity imaging is a novel domain which is currently gaining significant interest in the medical field. Most inversion techniques are based on the homogeneity assumption, i.e. the local spatial derivatives of the complex-shear modulus are ignored. This analysis presents an analytic approach in order to overcome this limitation, i.e. first order spatial derivatives of the real-part of the complex-shear modulus are taken into account. Resulting distributions in a gauged breast lesion phantom agree very well with the theoretical expectations. An in-vivo example of a cholangiocarcinoma demonstrates that the new approach provides maps of the viscoelastic properties which agree much better with expectations from anatomy.

© 2010 Académie des sciences. Published by Elsevier Masson SAS. All rights reserved.

1. Introduction

Tissue mechanics is clearly altered due to pathological changes. Therefore, manual palpation has been used for millennia in the diagnostic process for many diseases. Manual palpation is nowadays an integral part in the domains of, for instance, breast cancer, prostate cancer and liver fibrosis. When discussing the notion of tissue elasticity, it is important to specify which physical parameter exactly is measured: tissue consists of approximately 70% of water. Since water is mechanically incompressible, the compressional modulus λ is consequently not well suited to identify any structural change of tissue. On the other hand, water can easily be sheared. Therefore the shear modulus G_d of tissue is well suited to reveal subtle changes in its structural integrity. This has been shown for instance for liver fibrosis, where shear modulus imaging has demonstrated the ability to assess non-invasively the grade of fibrosis [1–3]. Initial clinical results on larger patient groups also show great potential for breast cancer characterization [4–6], and first results also indicate that neuro-degenerative diseases like Alzheimer or Multiple Sclerosis lead to changes in brain tissue mechanics [7–9].

Elasticity imaging relies on the fact that the propagation properties of a mechanical wave are determined by the underlying mechanical tissue properties. A given mechanical wave at a certain frequency will travel faster in a stiff material and slower in a soft material. Using motion sensitive imaging techniques like MRI or Ultrasound, it is possible to follow the propagation of the wave non-invasively inside the patient. The "art" of elasticity imaging is hence to properly convert the local displacement information into mechanical properties, i.e. to calculate the complex-valued and frequency dependent shear modulus $G^*(\omega) = G_d(\omega) + iG_l(\omega)$, with the imaginary part G_l accounting for loss effects. Most approaches use the so-called homogeneity approximation: here it is assumed that the spatial derivatives of G^* are negligible in the vicinity of the spatial point where G^* shall be calculated, i.e. it is assumed that the complex-shear modulus is locally constant [10–12]. As will be shown later, this assumption simplifies greatly the inverse problem, but certainly leads to biases at edges. The aim of this analysis is to present a novel approach in order to take first order spatial derivatives of the real-part of G^* into

---

account. After the analytic part, results from 3D MR-elasticity imaging are presented for a gauged phantom and afterwards in-vivo results from a liver tumour.

2. Theory

The propagation of a monochromatic mechanical wave in a linear isotropic viscoelastic material is given by

$$\underbrace{-\rho\omega^2 u_i}_{\text{force-term}} = \underbrace{\partial_{x_k}\big(G^*\partial_{x_k}u_i\big)}_{\text{shear-term}} + \underbrace{\partial_{x_i}\big([\lambda + G^*]\partial_{x_k}u_k\big)}_{\text{mixing/compressional-term}} \tag{1}$$

with ρ the density of the material, ω the circular frequency, u_i the i's component of the 3D displacement vector $\vec{u}$, λ the compressional modulus and Einstein convention assumed for identical indices. Since we intend to apply this equation to tissue and use vibration frequencies of the order of 100 Hz, it is important to keep several physical conditions in mind:

1. Tissue is almost incompressible. Thus, λ is of the order of GPa which leads to a speed of sound of approximately 1550 m/s in tissue almost independent of the frequency [13];
2. Shear waves are slow (1–10 m/s) which cause G^* to be of the order of kPa, i.e. 6 orders of magnitude smaller than λ;
3. The term $\partial_{x_k}u_k$ represents the relative volume change and is consequently of very small magnitude in tissue [14];
4. Longitudinal waves are not attenuated when operating at frequencies of the order of 100 Hz [13]. Therefore λ is real-valued. Contrarily, shear waves are attenuated in this frequency range and G^* is complex-valued.

The small magnitude of the $\partial_{x_k}u_k$-term often leads to the wrong assumption that it might be possible to simply ignore the entire second term on the right-hand side of Eq. (1). This is however not correct. As can be seen in [15], when considering the limit of an incompressible material (i.e. the Poissons ratio σ approaches 0.5), the small magnitude of the $\partial_{x_k}u_k$-term is balanced by the large magnitude of the compressional modulus (which approaches infinity in case of incompressibility) leading to a so-called pressure term, i.e.

$$p = \lambda\partial_{x_k}u_k \tag{2}$$

which is non-zero even when assuming the material to be incompressible. Below, it will be shown how to calculate this pressure term.

Normally, the spatial derivatives of the material properties are ignored which lead to the following simplified equation:

$$-\rho\omega^2 u_i = G^*\nabla^2 u_i + \partial_{x_i}p \tag{3}$$

In order to eliminate the unknown pressure component, we apply the curl operator $\varepsilon_{rsi}\partial_{x_s}$ to both sides of Eq. (3) leading to a simple Helmholtz-type equation

$$-\rho\omega^2 q_r = G^*\nabla^2 q_r, \quad q_r = \varepsilon_{rsi}\partial_{x_s}u_i \tag{4}$$

which can be solved analytically at each point within the imaging volume because the curl of the displacement vector $\vec{u}$ can be calculated, for the density ρ a value corresponding to water is assumed and the vibration frequency ω is known from the experimental conditions. This way, the complex-shear modulus G^* can be calculated independently from any rheological model [16]. Its frequency dependence can be obtained by repeating the monochromatic experiment at different frequencies. In order to estimate the pressure term and prove its importance, it is now possible (once G^* has been calculated via Eq. (4)) to return to Eq. (3) and solve for the gradient-pressure-term, i.e.

$$\partial_{x_i}p_i = -\rho\omega^2 u_i - G^*\nabla^2 u_i \tag{5}$$

and recover the spatial distribution of $p(\vec{x})$ via integration. This distribution is lacking the DC value for the pressure p_0 but will clearly demonstrate the fact that the distribution of $p(\vec{x})$ is non-zero in tissue.

Solving Eq. (4) will certainly lead to biases in areas where the spatial derivatives of G^* are not negligible. Since Eq. (1) contains only first order derivatives of the viscoelastic material properties, we will consider only the linear derivatives of the real-part of G^*, i.e. we assume that $G^* = G_{d0} + \alpha_p x_p + iG_{l0}$ with α_p local constants describing the spatial variation of G_d. Thus, when applying the curl operator to Eq. (1) we obtain the following equation:

$$-\rho\omega^2 q_r = \underbrace{\big(\varepsilon_{rsi}\partial_{x_s}\partial_{x_k}G^*\big)}_{\ll 1}(\partial_{x_k}u_i) + \big(\partial_{x_k}G^*\big)(\partial_{x_k}q_r) + \big(\varepsilon_{rsi}\partial_{x_s}G^*\big)\nabla^2 u_i + G^*\nabla^2 q_r$$

$$+ \underbrace{\big(\varepsilon_{rsi}\partial_{x_s}\partial_{x_i}[\lambda + G^*]\big)}_{\sim 1}\underbrace{(\partial_{x_k}u_k)}_{\ll 1} + \underbrace{\big(\partial_{x_i}[\lambda + G^*]\big)}_{\sim 1}\underbrace{\big(\varepsilon_{rsi}\partial_{x_s}\partial_{x_k}u_k\big)}_{\ll 1}$$

$$+ \underbrace{\big(\varepsilon_{rsi}\partial_{x_s}[\lambda + G^*]\big)}_{\sim 1}\underbrace{(\partial_{x_i}\partial_{x_k}u_k)}_{\ll 1} + \underbrace{[\lambda + G^*]}_{\gg 1}\underbrace{\big(\varepsilon_{rsi}\partial_{x_s}\partial_{x_i}\partial_{x_k}u_k\big)}_{\equiv 0} \tag{6}$$

Obviously, most terms vanish either

- due to the restrictions that only linear terms for the spatial variation of G_d are considered,
- due to the small magnitude of the $\partial_{x_k} u_k$-term not being balanced by a term of large magnitude, or
- due to the fact that the curl of a grad-div-term is identical to zero.

Eq. (6) can thereby be written as:

$$-\rho\omega^2 q_r = \alpha_k(\partial_{x_k} q_r) + (\varepsilon_{rsi}\alpha_s)\nabla^2 u_i + (G_{d0} + iG_{l0})\nabla^2 q_r \tag{7}$$

which can be solved locally because q_r is complex-valued. Thus, there are in total 6 equations and 5 unknowns, i.e. G_{d0}, G_{l0}, α_i. It could and would certainly desirable to also solve for the spatial derivatives of the imaginary part of G^*. With single frequency data this is, however, not possible using a local ansatz for the inversion.

3. Material and methods

MR-elastography was used for the acquisition of the 3D volumetric displacement data. The details of this method are described elsewhere [10]. Briefly, MR-elastography yields, within a volume of the object, the amplitude and the phase of the 3D displacement field generated by a steady-state monochromatic vibrational source. For the phantom experiments, a gauged breast lesion phantom was used with an isotropic image resolution of 2 mm^3 and 200 Hz of vibration frequency [17]. In-vivo liver results were obtained from a selected patient who was diagnosed having a cholangiocarcinoma. Here, image resolution is 4 mm^3 and the vibration frequency is 50 Hz. The transducer producing the mechanical vibrations was placed one the right side of the patient pressing against the rib cage. It was driven in longitudinal mode, i.e. the vibrating piston pushed against the ribs.

4. Results

Figs. 1A–H show the results obtained in the breast lesion phantom. The phantom consists of an outer softer layer and an inner stiffer layer (Fig. 1A). In addition, two circular, yet stiffer, lesions are present in the selected slice (red and green circles). The corresponding images of G_d and G_l as obtained from the simple Eq. (4) are shown in Figs. 1B, C. The different compartments of the phantom are well visible and the obtained values for G^* agree with the expected values [18]. As mentioned before, this inversion does not take any local changes of the complex-shear modulus into account but assumes local homogeneity. When using instead Eq. (7) for the local inversion, interestingly we obtain similar maps for G_{d0} and G_{l0} (Figs. 1D, E) as previously for G^* when using Eq. (4). The corresponding images of α_x, α_y, α_z (Figs. 1F–H) clearly show the areas of spatially changing shear modulus (see Fig. 1A). In homogeneous regions of the phantom $\alpha_i \approx 0$ is registered as expected from theory. Steep changes of up to 1 kPa/mm are visible at material boundaries with the correct signs for the α_i's. When for instance regarding Fig. 1F and moving from left to right (i.e. towards the positive x-direction), we register

- at entry from outer layer into the inner layer $\alpha_x > 0$,
- at entry into the first lesion $\alpha_x > 0$,
- at exit from the first lesion $\alpha_x < 0$,
- at entry into the second lesion $\alpha_x > 0$,
- at exit from the second lesion $\alpha_x < 0$, and
- at exit from the inner layer into the outer layer $\alpha_x < 0$.

Similar effects are seen for α_y as well as for α_z. α_z is particularly interesting, because the left lesion is actually growing towards positive z-direction (hence $\alpha_z > 0$) while the right lesion is shrinking towards positive z-direction (hence $\alpha_z < 0$) since their positions are not symmetric with respect to the selected imaging plane.

Figs. 2A–I show the corresponding results as obtained for an in-vivo liver cancer case. The case consists of a large cholangiocarcinoma located within the red ROI (Fig. 1A) which has an outer strongly enhancing ring-like zone and a fibrotic/partially necrotic center (green ROI). This inner structure of the tumour becomes apparent when analyzing at the relative contrast agent (CA) enhancement pattern of the lesion (Fig. 2B). CA enhancement of the outer zone is about 100% after 5 min of bolus injection (relative to the native image before CA injection) while the central zone enhances only about 60%. Fibrotic/necrotic tissue is expected to be stiff and viscous. This, however, is not well visible when considering the images produced via utilization of Eq. (4), i.e. the equation assuming local homogeneity. The fibrotic core appears only shallowly stiff and little viscous (Figs. 2C, D). This changes dramatically when using Eq. (7) for the calculation of the complex-shear modulus. Now, the core of the lesion appears very stiff (Fig. 2E) and very viscous (Fig. 2F). The corresponding images of the spatial derivatives of $G_d(\vec{x})$ reveal the rather complex inner architecture of the lesion with strong spatial gradients present around the central zone (mind that the y-direction is flipped compared to Fig. 1). It is important to realize that the maps of G^* as obtained with Eq. (4) (Figs. 2C, D) yield very similar results outside the lesion when compared to the maps obtained for G^* using Eq. (7). This is an important check for the validity of Eq. (7).
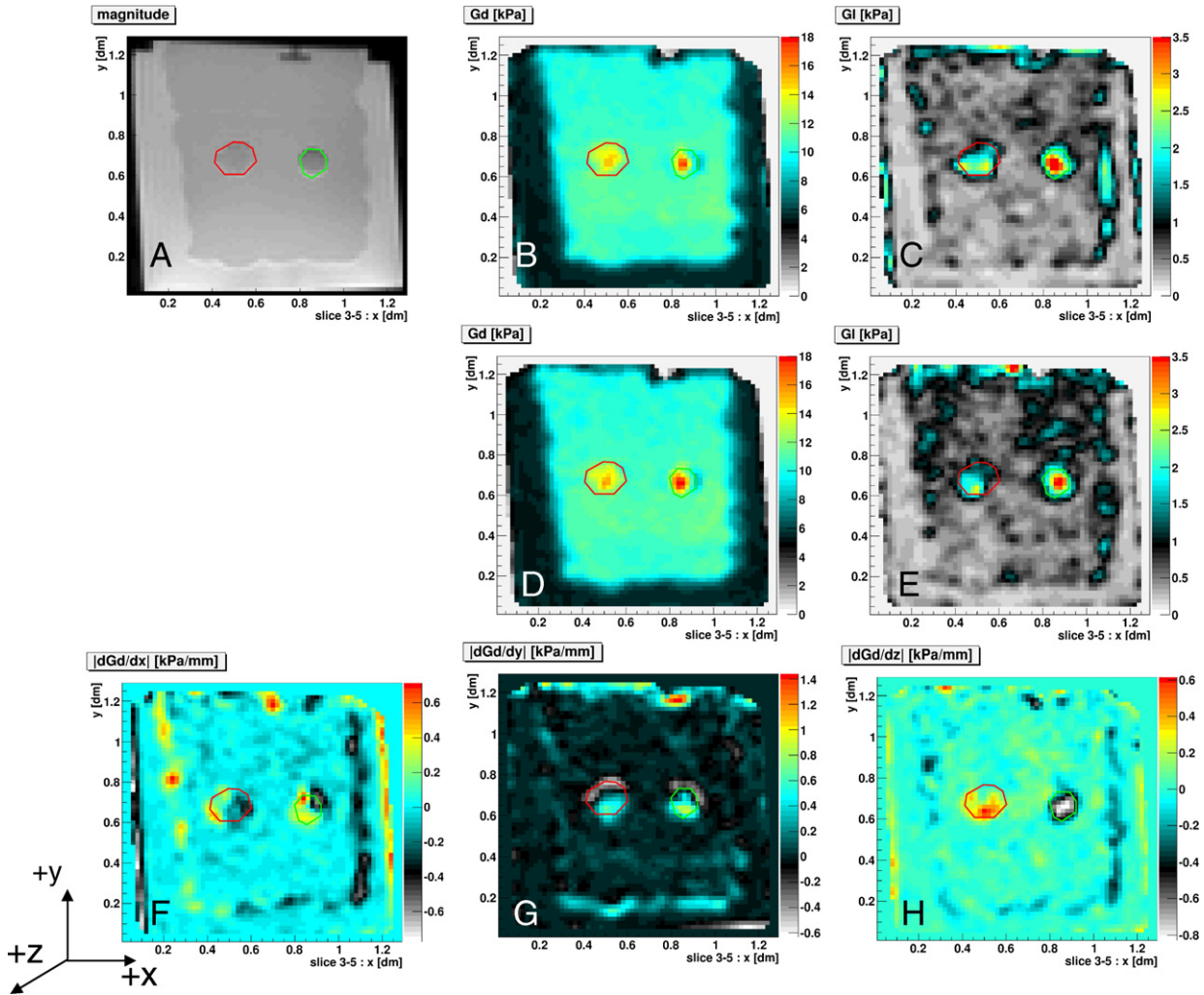
Fig. 1. Phantom results. A: MR-magnitude image depicting the different compartments of the phantom. B, C: G_d and G_l as calculated from Eq. (4). D, E: G_{d0} and G_{l0} as calculated from Eq. (7). F, G, H: spatial derivatives of the real-part of G^*. All values are in units of kPa.

Finally, we present in Fig. 3 the magnitude distribution of the complex-valued pressure $p(\vec{x})$ for the in-vivo case as obtained from Eq. (5). Mind that the DC is missing. The distribution reveals a spatially dependent pressure field with a maximum close to the position of the transducer (upper left region in Fig. 3). There, peak values of about 0.16 kPa are registered. This example clearly demonstrates that the assumption of a constant pressure distribution is not valid and that the spatial dependence of this field can be very complex.

5. Discussion and conclusions

Elasticity imaging is a novel emerging field which attracts currently a lot of interest in the medical community. Intuitively it is obvious that mechanical parameters carry a large potential for the identification and characterization of pathological changes in tissue. Initial clinical studies in the domains of liver, breast and brain clearly demonstrate the enormous potential behind this technique.

In order to measure viscoelastic properties of tissue, it is necessary to send a mechanical wave into the object and measure the propagation properties of the wave. Utilization of Eq. (1) allows then to reconstruct images of the complex-valued shear modulus G^*. As always, there are different approaches in order to do so: the direct approach by simply solving locally Eq. (1) [10] or the indirect approach via for instance FEM methods [19]. In this analysis we followed the direct approach in order to high-light the important physical constraints. The fundamental difficulty faced within tissue is the large difference in magnitude between the shear modulus and the compressional modulus which has its origin in the fact that tissue is almost incompressible. Hence, the $\partial_{x_k} u_k$-term (relative volume change) in Eq. (1) is of very small magnitude and cannot be calculated from the data obtained via MR-elastography due to SNR and image resolution limitations. Thus, solving this equation by using the measured displacement data is simply not possible. Forward FEM simulations also face
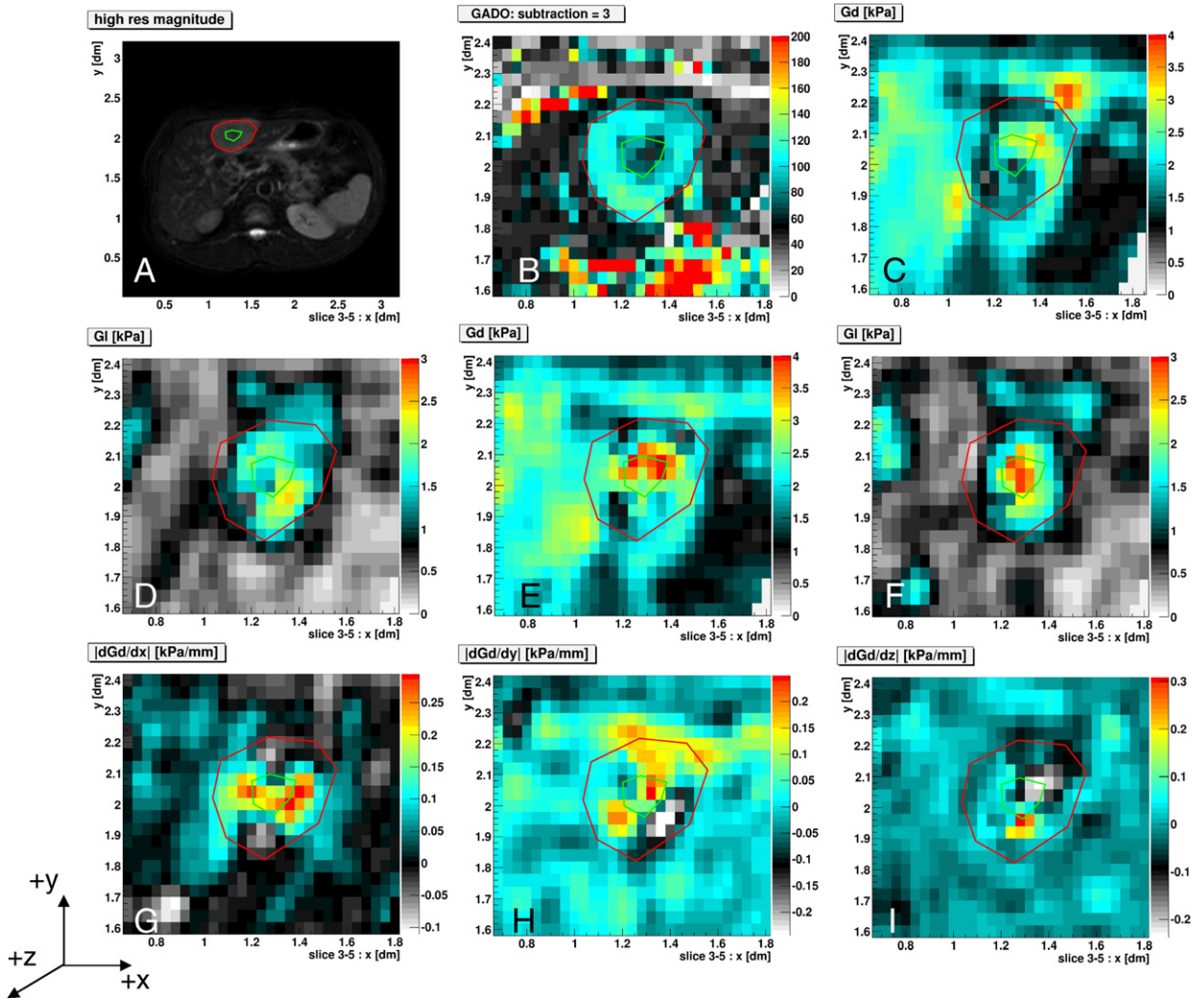
Fig. 2. In-vivo results. A: MR-magnitude image of the abdomen showing the liver with the lesion (red ROI). B: relative enhancement pattern of contrast agent after 5 min of bolus injection in percent. C, D: G_d and G_l as calculated from Eq. (4). E, F: G_{d0} and G_{l0} as calculated from Eq. (7). G, H, I: spatial derivatives of the real-part of G^*. All values are in units of kPa.
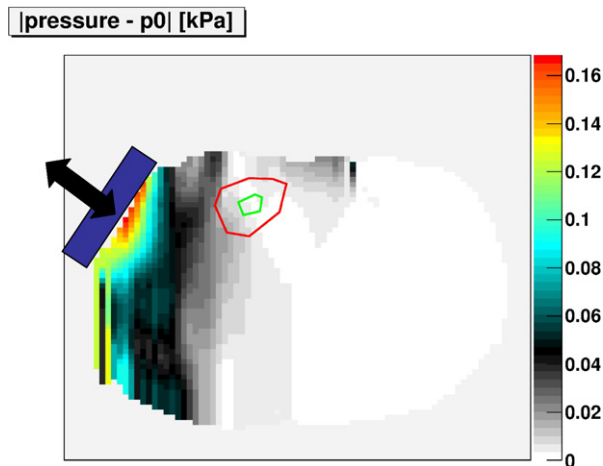

Fig. 3. Magnitude distribution of the complex-valued pressure distribution for the in-vivo case as calculated from Eq. (5) in units of kPa. The location of the mechanical transducer is indicated by the blue rectangle in the upper left corner. The black double-arrow shows the direction of vibration.

severe issues of stability once using correct values for the speed of the compressional wave (1550 m/s compared to 1–10 m/s for the shear wave). As clearly shown in Fig. 3, the pressure term arising from the combination of the compressional modulus λ and the $\partial_{x_k} u_k$-term is not negligible and contributes by up to 10% to the shear modulus (mind that the DC is not known here, so the true contribution can only become larger). In order to overcome this dilemma, utilization of the curl operator has been proposed [16]. This introduces another spatial derivative which requires data of sufficiently high SNR fortunately provided by MR-elastography. Other methods have also been proposed like for instance low-pass filters [20]. Here, we want to follow a physically motivated approach in order to clearly identify the consequences of trying to suppress contributions from the compressional wave. Different approaches can now be followed when applying the curl operator to Eq. (1): neglecting the spatial derivatives of the material distribution (leading to Eq. (4)) or taking them into account (leading to Eq. (7)). Most of the terms in Eq. (6) can be neglected due to the small magnitude of the $\partial_{x_k} u_k$-term and the fact that spatial derivatives of λ are of small magnitude compared to the large magnitude of λ itself. Also the assumption of considering only first order spatial derivatives simplifies considerably the number of unknown parameters.

The results obtained in the breast phantom (Fig. 1) show two things:

1. utilization of Eq. (4) yields high-quality maps of the complex-shear modulus with values in agreement with data obtained from rheometers [18], and
2. utilization of Eq. (7) does not significantly improve the results. Maps of the spatial derivatives of $G_d(\vec{x})$ (i.e. the α_i) clearly show the presence of boundaries in elasticity contrast.

It should be noted that the phantom consists of rather simple objects which have no further internal structure. This does not hold for the presented in-vivo case of a cholangiocarcinoma. Here, utilization of Eq. (7) clearly improves the anatomical correspondence between the expected internal structures as seen on gadolinium contrast enhanced MR-images and obtained maps for the complex-shear modulus (Fig. 2). Here, the maps for α_i reveal a very complex internal structure of the lesion. It should be noted that Eq. (7) does not add any additional spatial derivatives to the data and that both equations are over-determined, i.e. in case of Eq. (4) we have two unknowns and 6 equations while in case of Eq. (7) we have 5 unknowns with still 6 equations. Both equations use 3rd order spatial derivatives of the displacement vector $\vec{u}(x)$ which is certainly challenging. Other integral approaches might certainly yield more stable results [19] but face the problem of boundary conditions which are most difficult to assess for data like those presented in Fig. 2. It would certainly be desirable to also take spatial derivatives of G_l into account, but this would introduce three more unknowns. One possibility to solve this problem would be the utilization of 2 datasets with slightly different frequencies or source configurations. Thereby, 12 equations were available which would allow solving for the 8 unknown parameters.

Another important finding of this analysis is that the pressure-term (Eq. (5)) can firstly be calculated from MR-elastography data and that the spatial distribution of this pressure is neither negligible nor spatially constant. Hence solving Eq. (1) by just ignoring the entire mixing-term will lead to biased data [11]. Having now calculated the pressure-term, it would certainly be interesting to study the spatial distribution of λ by simply dividing the integrated Eq. (5) by the $\partial_{x_k} u_k$-term. Unfortunately, this is currently not possible because of the significant errors present when calculating $\partial_{x_k} u_k$. Future work will be dedicated to ways of solving this issue in order to gain insight into the variation of the compressional properties of tumours.

References

[1] L. Huwart, F. Peeters, R. Sinkus, L. Annet, N. Salameh, L.C. ter Beek, Y. Horsmans, B.E. Van Beers, NMR Biomed. 19 (2) (2006 April) 173–179.
[2] O. Rouvière, M. Yin, M.A. Dresner, P.J. Rossman, L.J. Burgart, J.L. Fidler, R.L. Ehman, Radiology 240 (2) (2006 August) 440–448.
[3] L. Huwart, C. Sempoux, E. Vicaut, N. Salameh, L. Annet, E. Danse, F. Peeters, L.C. ter Beek, J. Rahier, R. Sinkus, Y. Horsmans, B.E. Van Beers, Gastroenterology 135 (1) (2008 July) 32–40, Epub 2008 April 4.
[4] A.L. McKnight, J.L. Kugel, P.J. Rossman, A. Manduca, L.C. Hartmann, R.L. Ehman, AJR Am. J. Roentgenol. 178 (6) (2002 June) 1411–1417.
[5] R. Sinkus, K. Siegmann, T. Xydeas, M. Tanter, C. Claussen, M. Fink, Magn. Reson. Med. 58 (6) (2007 December) 1135–1144.
[6] K.C. Siegmann, T. Xydeas, R. Sinkus, B. Kraemer, U. Vogel, C.D. Claussen, Eur. Radiol. 20 (2) (2010 February) 318–325.
[7] I. Sack, B. Beierbach, J. Wuerfel, D. Klatt, U. Hamhaber, S. Papazoglou, P. Martus, J. Braun, Neuroimage 46 (3) (2009 July 1) 652–657.
[8] E. Diguet, B. Larrat, R. Sinkus, M. Fink, in: Proceedings of International Tissue Elasticity Conference, 2009, The Netherlands, #059.
[9] J. Wuerfel, F. Paul, B. Beierbach, U. Hamhaber, D. Klatt, S. Papazoglou, F. Zipp, P. Martus, J. Braun, I. Sack, Neuroimage 49 (3) (2010 February 1) 2520–2525.
[10] R. Sinkus, J. Lorenzen, D. Schrader, M. Lorenzen, M. Dargatz, D. Holz, Phys. Med. Biol. 45 (6) (2000 June) 1649–1664.
[11] T.E. Oliphant, A. Manduca, R.L. Ehman, J.F. Greenleaf, Magn. Reson. Med. 45 (2) (2001 February) 299–310.
[12] S. Papazoglou, U. Hamhaber, J. Braun, I. Sack, Phys. Med. Biol. 53 (12) (2008 June 21) 3147–3158.
[13] F. Duck, Physical Properties of Tissue, Academic Press, London, 1990.
[14] L. Landau, E. Lifschitz, Theory of Elasticity, 3 edition, Butterworth–Heinemann, 1986.
[15] R. Sinkus, M. Tanter, S. Catheline, J. Lorenzen, C. Kuhl, E. Sondermann, M. Fink, Magn. Reson. Med. 53 (2) (2005 February) 372–387.
[16] R. Sinkus, M. Tanter, T. Xydeas, S. Catheline, J. Bercoff, M. Fink, Magn. Reson. Imaging 23 (2) (2005 February) 159–165.
[17] E.L. Madsen, M.A. Hobson, G.R. Frank, et al., Ultrasound Med. Biol. 32 (6) (2006) 857–874.
[18] R. Sinkus, K. Siegmann, T. Xydeas, M. Tanter, C. Claussen, M. Fink, Magn. Reson. Med. 58 (6) (2007 December) 1135–1144.
[19] E.V. Houten, J. Weaver, M. Miga, F. Kennedy, K. Paulsen, Med. Phys. 27 (1) (2000) 101–107.
[20] A. Manduca, D.S. Lake, S.A. Kruse, R.L. Ehman, Med. Image Anal. 7 (4) (2003 December) 465–473.